Geomorphology 492 (2026) 110057

Contents lists available at ScienceDirect

Geomorphology

journal homepage: www.journals.elsevier.com/geomorphology

A giant Early Holocene tsunamigenic rock-ice avalanche in South Greenland preconditioned by glacial debuttressing

L.L. Pedersen [a,b,*], K. Svennevig [b], C. Morino [c], A.S. Søndergaard [d], C. Pearce [a,e], L.F. Pérez [b], A. Damsgaard [b], J. Olsen [f], M.F. Knudsen [a], A. Noblet [g], N.K. Larsen [h]

[a] Department of Geoscience, Aarhus University, Høegh-Guldbergs Gade 2, 8000 Aarhus C, Denmark
[b] Geological Survey of Denmark and Greenland – GEUS, Øster Voldgade 10, 1350 Copenhagen, Denmark
[c] Department of Land, Environment, Agriculture and Forestry, University of Padova, Italy
[d] Laboratory of Ion Beam Physics, Department of Physics, ETH Zürich, Otto-Stern-Weg 5, 8093 Zürich, Switzerland
[e] Department of Geoscience, Arctic Research Centre, iClimate Centre, Aarhus University, Høegh-Guldbergs Gade 2, 8000 Aarhus C, Denmark
[f] Aarhus AMS Centre (AARAMS), Department of Physics and Astronomy, Aarhus University, Ny Munkegade 120, 8000 Aarhus C, Denmark
[g] Department of Earth Sciences, University of Western Ontario, Canada
[h] Section for Geogenetics, Globe Institute, University of Copenhagen, Øster Voldgade 5-7, DK-1350 Copenhagen, Denmark

ARTICLE INFO

Keywords:
Rock-ice avalanche
Glacial debuttressing
^{10}Be cosmogenic nuclide exposure dating
Tsunamigenic rock-slope failure

ABSTRACT

Deposits of a giant (more than 1 km^3) rock-ice avalanche with a runout of 15.8 km and an associated failure scar have been discovered in Tupaasat Valley, South Greenland (*Kalaallit Nunaat*). To study its formation, a geomorphological map of the area has been produced using mainly remote sensing, while the age of the landforms has been constrained based on ^{10}Be cosmogenic nuclide exposure dating. The rock-ice avalanche landforms include a 1100 m wide mound of displaced material located approximately 6.4 km from the scar, at a change in slope from around 4° to 1.5°. A boulder field containing boulders up to 45 m across lies 0.5 km farther down the valley. Beyond the boulder field are kettle holes up to 45 m in diameter and debris cones interpreted as molards reaching heights up to 36 m and diameters up to 140 m. The source area of the rock-ice avalanche is on a mountain crest above a present-day glacier. The rock-ice avalanche landforms yielded ^{10}Be ages ranging from c. 12.3 to 9.5 ka with a weighted mean of 10.9 ± 0.5 ka, which coincides with the generally known deglaciation age of the valley. Based on our results, we suggest that the rock-ice avalanche was preconditioned by glacial debuttressing during the deglaciation of the valley and created a tsunami when it impacted a nearby fjord. Such events are expected to be more frequent due to climate change and future ice loss and pose a hazard for populations located near glaciated valleys. A better understanding of past events can help mitigate future large rock-slope failures.

1. Introduction

Rock avalanches preconditioned by glacial debuttressing pose a significant geohazard (Kos et al., 2016; Fey et al., 2017; Tapia Baldis and Trombotto Liaudat, 2019; Dai et al., 2020; Svennevig et al., 2024a). With increasing loss of ice from glaciers, the risk to humans and their settlements in areas prone to these types of rock-slope failures continues to grow (Saemundsson et al., 2022). Improving the understanding of both the preconditioning factors and the consequences of such events will help in adapting to and thus reducing the risk. Studying past and present rock avalanches helps us understand and possibly identify future occurrences and assess secondary impacts like outburst floods and tsunamis (also termed displacement waves, e.g. Hermanns et al. (2013)). For these reasons, it is important to study cases of past events (e.g. Borgatti and Soldati, 2010; Matthew et al., 2024; Svennevig et al., 2024b).

Rock avalanches are large, destructive rock-slope failures with high mobility that can drastically modify the landscape and generate tsunamis if they impact water bodies, particularly in topographically constrained locations such as fjords (Deline, 2009; Hungr et al., 2014;

* Corresponding author.
E-mail addresses: lyngkjaer.mail@gmail.com (L.L. Pedersen), ksv@geus.dk (K. Svennevig), costanza.morino@gmail.com (C. Morino), anneso@phys.ethz.ch (A.S. Søndergaard), christof.pearce@geo.au.dk (C. Pearce), lfp@geus.dk (L.F. Pérez), andam@geus.dk (A. Damsgaard), jesper.olsen@phys.au.dk (J. Olsen), mfk@geo.au.dk (M.F. Knudsen), anoblet@uwo.ca (A. Noblet), nicl@sund.ku.dk (N.K. Larsen).

https://doi.org/10.1016/j.geomorph.2025.110057
Received 17 January 2025; Received in revised form 15 July 2025; Accepted 11 October 2025
Available online 20 October 2025

Hermanns et al., 2021). The mobility of a rock avalanche increases systematically with mass and volume (Scheidegger, 1973; Hermanns et al., 2021). Deposits from paleo-rock avalanches can be difficult to identify due to reworking by other processes, such as glacial advances and fluvial processes (Cook et al., 2013). However, they may be recognizable in the landscape by the deep scarp they create in the hillslopes or from the presence of diagnostic depositional landforms.

In glaciated regions, rock avalanches are becoming more frequent as temperatures rise due to climate change (Cossart et al., 2008; Fey et al., 2017; Coe et al., 2018). Central West Greenland is an example of an area where climate-related rock avalanches have occurred (Svennevig et al., 2020, 2022, 2023, 2024b). Several factors can precondition rock avalanches in Arctic settings, including glacial debuttressing and permafrost degradation (Tapia Baldis and Trombotto Liaudat, 2019; Saemundsson et al., 2022; Cathala et al., 2024). Glacial debuttressing occurs when glaciers retreat and the adjacent rock slopes then potentially become destabilized as the state of stress within the slope is altered, which increases the likelihood of rockslides, rock avalanches or landslides (Ballantyne, 2002; Kos et al., 2016; Svennevig et al., 2024a). Glacial erosion of the bedrock during glacial cycles may also play a role in weakening the rock slope (Grämiger et al., 2017). If a rock avalanche involves a glacier, its mobility is further enhanced because snow and ice reduce the coefficient of friction, leading to longer runouts (Deline, 2009; Reznichenko et al., 2011). Additionally, entrainment of sediment, snow and ice in the rock avalanche can occur and possibly increase its mobility and transform the rock avalanche into a rock-ice avalanche. Such events commonly occur in high mountainous regions, such as the Upper Durance catchment, France (Cossart et al., 2008), the Mont Blanc massif, France (Deline, 2009), Saint Elias Mountains, Alaska (Bessette-Kirton and Coe, 2020), Pizzo Cengalo, Switzerland (Walter et al., 2020) and in Chamoli, India (Shugar et al., 2021), but have also recently been described from East Greenland fjords (Svennevig et al., 2024a).

During a Greenland-wide landslide mapping (Svennevig, 2019), a large rock avalanche scarp and deposit was identified in the Tupaasat Valley, South Greenland, here termed the Tupaasat rock-ice avalanche. This sparked the questions of when the rock-ice avalanche occurred, what could have caused such a large magnitude event, and whether it was tsunamigenic. In this study, we combine detailed geomorphological mapping using remote sensing data and cosmogenic nuclide dating of key landforms to enhance our understanding of the Tupaasat rock-ice

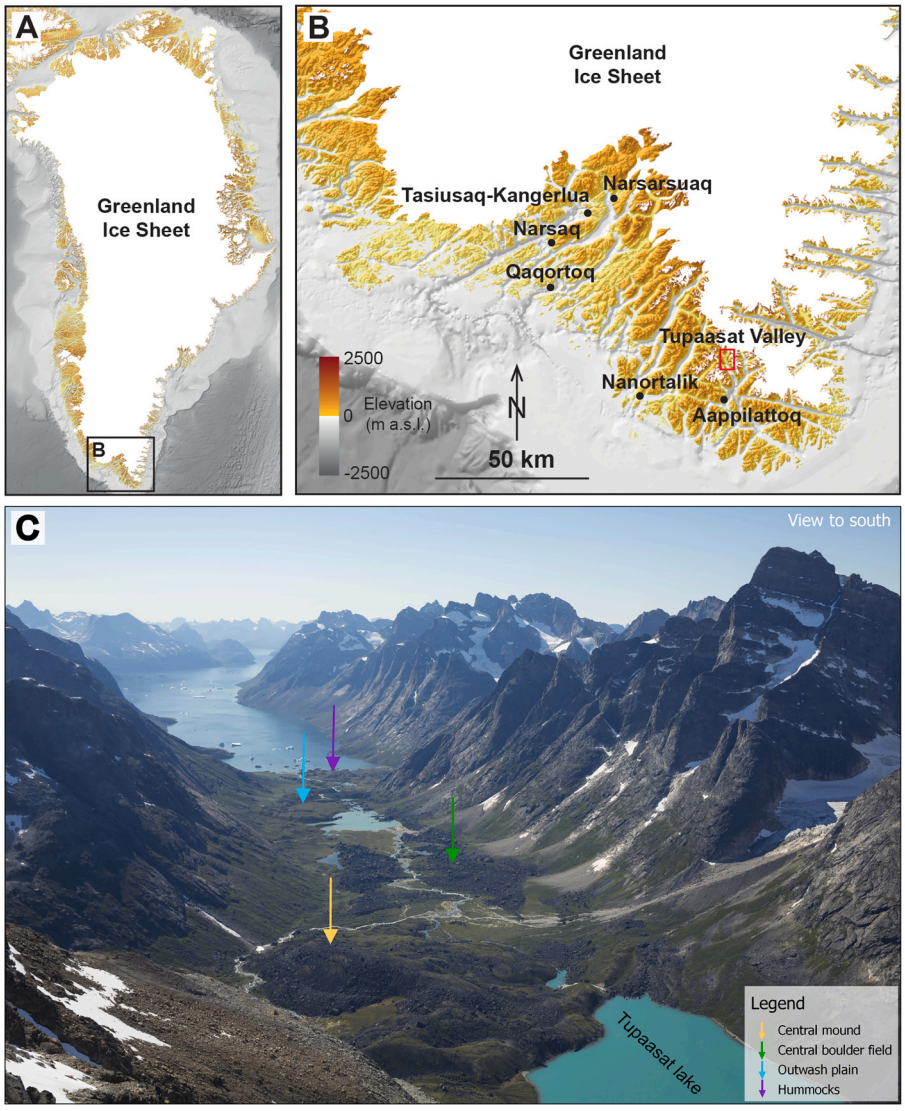

Fig. 1. A) Map showing the location of the study area, Tupaasat Valley, in South Greenland. B) Map of the outline in A with larger settlements named and the study area marked by the red box. Topographic data from BedMachine Greenland v4 (Morlighem et al., 2021) and ArcticDEM (Porter et al., 2022). C) Oblique view of Tupaasat Valley and Tupaasat lake looking towards the south, with arrows pointing at the main landforms: central mound, central boulder field, outwash plain, and hummocks terminating into the fjord. (Photo: Tilmann Graner).

avalanche and discuss potential preconditioning factors and implications.

2. Geological and geomorphological settings

Tupaasat Valley is located in South Greenland (60°24'43"N, 44°16'52"W) in close proximity to the present-day ice margin of the Greenland Ice Sheet (GrIS) and 25 km E-NE of Nanortalik (Fig. 1). The U-shaped valley is c. 1 km wide and stretches for c. 12 km continuing towards the south into the narrow Kangikitsoq Fjord which is 74 km long and more than 500 m deep. The relief in the valley bottom is gently inclined from sea level to approximately 500 m above sea level (a.s.l.) at the valley head, where two glaciers merge up to 3.5 km from their source areas. The slopes of the valley are up to 44° steep with heights up to 1500 m a.s.l. Several small and receding glaciers are situated on the slopes. The bedrock in the area is mapped to be composed of rapakivi granite and paragneisses with a mix of metagreywacke, metasiltstone, and metamudstone (Escher and Pulvertaft, 1995; Garde, 2007). The isostatic adjustments and relative sea level (RSL) changes associated with the ice-marginal fluctuations in South Greenland have been reconstructed using mapping of raised marine deposits, landforms, and isolation basins at Tasiusaq-Kangerlua, Qaqortoq, and Narnortalik showing marine limits reaching 30–35 m a.s.l. (Bennike and Björck, 2002; Sparrenbom, 2006; Sparrenbom et al., 2006, 2013). Closer to the present-day ice margin, information on RSL is scarce and based on raised marine deposits indicating a marine limit of c. 10 m a.s.l. in Aappilattoq and Tupaasat Valley (Bøgvad, 1940; Weidick, 1987).

The glacial history of South Greenland is generally well-constrained. During the Last Glacial Maximum (LGM, 26–19 ka) the GrIS advanced to the shelf break (Funder et al., 2011). The ice thickness in the coastal areas exceeded 1500 m, thus, even the highest mountains were most likely ice-covered (Bennike and Björck, 2002; Andersen et al., 2020). Evidence from marine sediment cores indicates that the offshore continental shelf began to deglaciate around 19 ka before present (BP) (Carlson et al., 2008; Winsor et al., 2015). Cosmogenic surface exposure dating and minimum limiting ^{14}C dating suggest that the outer coastal areas in southern Greenland were deglaciated between 14.8 and 12.3 ka and the ice margin reached the present-day ice extent between 11.5 and 9.1 ka BP (Kaplan et al., 2002; Larsen et al., 2011; Levy et al., 2020; Andersen et al., 2020). The GrIS retreated inside its present extent in the Early and Middle Holocene until it began to readvance at the onset of the Neoglacial c. 5–4 ka BP which culminated with a maximum ice extent in most places during the Little Ice Age (LIA) c. 0.5–0.3 ka BP (Weidick et al., 2004; Larsen et al., 2016; Kjær et al., 2022). Local glaciers retreated in concert with the GrIS and became very small or completely disappeared in the Middle Holocene from c. 7.3 to 1.2 ka BP (Larocca et al., 2020). The glacial history in the Tupaasat Valley is constrained by Sinclair (2019), dating two identified moraines (inner and outer) in the valley. Early Holocene ages of 12.5 to 10 ka have been obtained by dating boulders on the outer moraine, next to the Tupaasat Lake, about 2 km from the present-day glacier front at the valley head (Fig. 1C). About 400 m farther up the valley, boulders on the inner moraine result in younger deglaciation ages of 0.8 ka. Thus, ice in the Tupaasat Valley followed the overall deglaciation pattern seen in southern Greenland (Sinclair, 2019).

3. Methods

3.1. Mapping

We produced a geomorphological map of the rock avalanche-affected area based on satellite images, DEMs, multibeam bathymetry, and oblique aerial photographs. Remote sensing observations were supplemented by photos from the study area collected during a half-day field visit focused on sampling for cosmogenic nuclide exposure dating of relevant landforms.

3.2. Digital elevation model

A 2 m DEM created from Pléiades stereo pairs from 2020 were used in the mapping. To correct it for true elevation, a 2 m DEM from the Danish Agency for Data Supply and Infrastructure (SDFI) was implemented in the QGIS software version 3.22.5. The SDFI DEM is based on satellite images collected in 2022 and has a high-accuracy elevation of 20–200 m, but relevant parts of the study area are missing (Agency for Climate Data, n.d.; Westoby et al., 2012). In addition, an orthophoto from SDFI, made from "Satellite pour l'Observation de la Terre" (SPOT) satellite images with a pixel size of 2 × 2 m, supported the morphological mapping. For the fjord, we created a 10 m resolution bathymetry model in QPS Qimera software from the multibeam bathymetry data obtained from the Danish Geodata Agency.

3.3. Morphometric analysis of hummocks

We measured the morphometric characteristics of hummocks found within the rock avalanche deposit. They were digitized as polygons in QGIS based on the texture in orthophotos and the elevation data. The area of the individual hummock was derived using the QGIS area-function in the field calculator. The height measurements were all performed in QGIS on the DEM using the 'Terrain profile' tool. We determined the landform height as the difference between the top elevation of the hummock and the mean elevation of the terrain surrounding the hummock. For each hummock, we measured the slope parallel and perpendicular to the rock avalanche runout direction. In addition, we calculated the radius parallel and perpendicular to the rock avalanche runout direction. From these, the radius ratio was calculated to define a dominating long axis. A sample area of individual hummocks was selected based on the spatial distribution of the hummocks, where the individual hummock is more isolated, and the central location in the deposits at the transition zone from land to water. This increases the accuracy of the measurements. We chose a sample area of 92 hummocks in the vicinity of the coast for the morphometric analyses to represent all the mapped rock avalanche-generated hummocks in the runout zone.

3.4. Rock avalanche volume calculation

A minimum volume estimate of the rock avalanche was calculated by closing the failure scarp on the mountain with two planes (dip/dip azimuth 45/278 and 35/100) parallel to the surrounding undisturbed mountainside. This gives a minimum estimate for the total mobilized volume as it does not account for landslipped material still residing inside that scarp, the bulking of the mobilized material as it fractured during transport and material entrained by the rock ice avalanche as it travelled down the valley (e.g. Hungr and Evans, 2004). A similar approach was employed by Svennevig et al. (2024b) for large paleo landslides in central West Greenland. The volume calculation was performed in the 3D-modelling software MOVE. The volume was then used to classify the size of the rock avalanche based on McColl and Cook (2024).

3.5. ^{10}Be exposure dating

Cosmogenic nuclide exposure dating can be used for a wide range of geological purposes, including constraining the timing of past rock avalanches (Ivy-Ochs and Kober, 2008). Samples for cosmogenic nuclide ^{10}Be exposure dating were collected during a single day of helicopter-supported reconnaissance in the summer of 2022. The samples were collected using a rock saw, hammer, and chisel. We sampled 6 boulders and cut out squares of the top c. 3–5 cm of each boulder (Table 1). Three boulders, approximately 1 m in height and with some lichen cover, were situated on top of a hummock at the valley mouth. Three boulders were located in the boulder field farther up the valley, all large blocks were 3–5 m high and with only sporadic lichen cover (Fig. 3A). We recorded

Table 1
Sample collection, ^{10}Be isotopic information and resulting exposure ages for 6 boulders from Tupaasat Valley, South Greenland.

Sample name	Elevation (m a.s.l.)	Latitude (°N)	Longitude (°W)	Sample thickness (cm)	Shielding correction	Quartz (g)	Carrier added (g)[a]	Sample ^{10}Be/^{9}Be ratio (10^{-14})	Blank ^{10}Be/^{9}Be ratio (10^{-14})	^{10}Be conc. (atoms/g)	^{10}Be unc (atoms/g)	^{10}Be age (ka)[b]
Boulders on top of molard												
GL2204	32	60.33	−44.27	5.0	0.945	24.9986	0.25054	6.41 ± 0.36	0.18 ± 0.06	39581	2337	9.5 ± 0.6 (1.0)
GL2205	28	60.33	−44.27	5.2	0.945	25.0306	0.24949	7.09 ± 0.58	0.18 ± 0.06	43674	3701	10.6 ± 0.9 (1.3)
GL2206	28	60.33	−44.27	4.9	0.945	25.0060	0.24997	8.23 ± 0.33	0.18 ± 0.06	50875	2152	12.3 ± 0.5 (1.2)
Boulders in block field												
GL2207	81	60.35	−44.28	3.2	0.865	25.0118	0.24995	7.82 ± 0.46	0.18 ± 0.06	48422	2961	11.9 ± 0.7 (1.2)
GL2208	89	60.35	−44.28	4.9	0.928	25.0155	0.24884	7.16 ± 0.40	0.18 ± 0.06	49488	2278	11.4 ± 0.5 (1.1)
GL2209	62	60.35	−44.28	4.8	0.936	25.0144	0.25054	7.84 ± 0.43	0.18 ± 0.06	44028	2572	10.3 ± 0.6 (1.1)
Total weighted mean age: 10.9 ± 0.5												

[a] Carrier *Phe1603* (949.4±6.2 μg ^{9}Be/g) was used for preparation of all samples.
[b] ^{10}Be ages were calculated using the online exposure age calculator formerly known as the CRONUS-Earth online exposure calculator v.3 (Balco et al., 2008), the Arctic production rate (Young et al., 2013), and the Lm scaling scheme (Lal, 1991; Stone, 2000) under standard atmosphere. Exposure ages calculated using other scaling schemes deviate by <2% and exposure ages calculated using the Baffin Bay production rate (Young et al., 2013) deviate by <1%. A rock density of 2.65 g cm^{-3} was used and we assumed zero erosion. Samples were normalized to the beryllium standard ICN-01-5-4, with a ^{10}Be/^{9}Be value of 2.851 × 10^{-12} (Nishiizumi et al., 2007) and blank corrected. ^{10}Be ages are presented with internal and external (brackets) uncertainties. The total weighted mean of all samples including external uncertainties are shown in bold.

the latitude, longitude, and elevation of each sample using a hand-held Garmin e-trex 30 GPS with an accuracy of 5–10 m. Shielding by the surrounding topography as well as the orientation of the rock surface were measured using a compass and clinometer. All boulders sampled were situated above the marine limit of the area (Bøgvad, 1940; Weidick, 1987). No geomorphological evidence of wave activity is found in the area, likely due to rapid isostatic uplift in the area. Rapid uplift after initial deglaciation is also seen around Qaqortoq, approximately 100 km northwest of the study area (Sparrenbom et al., 2006). For these reasons, we do not correct our calculations for post-retreat submergence. While the uplift possibly was rapid, it is not well constrained in the area and southern Greenland in general and we therefore have not made corrections for uplift in our calculations, following studies in Greenland that have shown this correction to be negligible (Sinclair et al., 2016; Larsen et al., 2018; Young et al., 2020).

In the laboratory, sample thicknesses were measured using a caliper to calculate the average sample thickness. The samples were then crushed and sieved to the 250–700 μm size fraction. Samples and one blank were processed and beryllium extracted at Aarhus University in the Cosmogenic Nuclide Laboratory at the Department of Geoscience, following methods adapted from (Corbett et al., 2016). ^{10}Be/^{9}Be ratios were measured at the Aarhus AMS Centre, Aarhus University. Nuclide concentrations were normalized to the beryllium standard ICN-01-5-4, with a ^{10}Be/^{9}Be value of 2.851 × 10^{-12} (Nishiizumi et al., 2007) and all samples were blank corrected. To calculate the ^{10}Be exposure ages we used the online exposure age calculator formerly known as the CRONUS-Earth online exposure calculator v.3 (Balco et al., 2008) with the Arctic production rate (3.96 ± 0.15 atoms g^{-1} a^{-1}) (Young et al., 2013) and the Lm production scaling scheme (Lal, 1991; Stone, 2000) under standard atmosphere conditions. Exposure ages calculated using other scaling schemes deviate by <2 % and exposure ages calculated using the Baffin Bay production rate (Young et al., 2013) deviate by <1 %. A rock density of 2.65 g cm^{-3} was used assuming zero erosion. We did not correct for cover by vegetation or snow, as the vegetation in the area is sparse, and the sampled boulders were positioned in open locations in the landscape with a low probability of long periods with snow cover. ^{10}Be exposure ages and information used for the calculations are found in Table 1, including both internal and external uncertainties. We further calculate a total weighted mean of all ^{10}Be samples, making sure the chi-square test was fulfilled. When calculating the total weighted mean, we include external uncertainties, which include the production rate and scaling uncertainties (Balco et al., 2008).

4. Results

4.1. Rock avalanche landforms

The rock avalanche has a total length of 15,830 m from the top of the scar to the most distal submarine hummocks imaged in the fjord, interpreted to be part of the rock avalanche deposit. The total drop height is 1440 m, and the average slope is 5°. This equates to a fahrböschung of 0.09 (Scheidegger, 1973; Hermanns et al., 2021). We identify several landforms related to the rock avalanche in Tupaasat Valley, such as a central mound, boulder fields, hummocks and circular depressions (Fig. 2A, B). We see no post-depositional reworking of the landslide deposit except from glacial activity in the source area inside the Little Ice Age moraine and from later fluvial activity (Geomorphological map of the entirety of the Tupaasat Valley is included in the Supplementary Information).

4.1.1. Rockslide source area

We have identified a large rockslide scarp on the mountain crest above the glacier using aerial photographs and DEMs (Fig. 3). The slide scar is east-facing and is 1.6 km deep from east to west and 2.3 km in length from north to south, covering an area of c. 2.7 km^2. As seen on the cross section (Fig. 2C), the slope of the source area is steepest from the present mountain crest at c. 1300 m a.s.l. down to around 800 m a.s.l. where it becomes flatter until around 700 m a.s.l. Here, a ridge

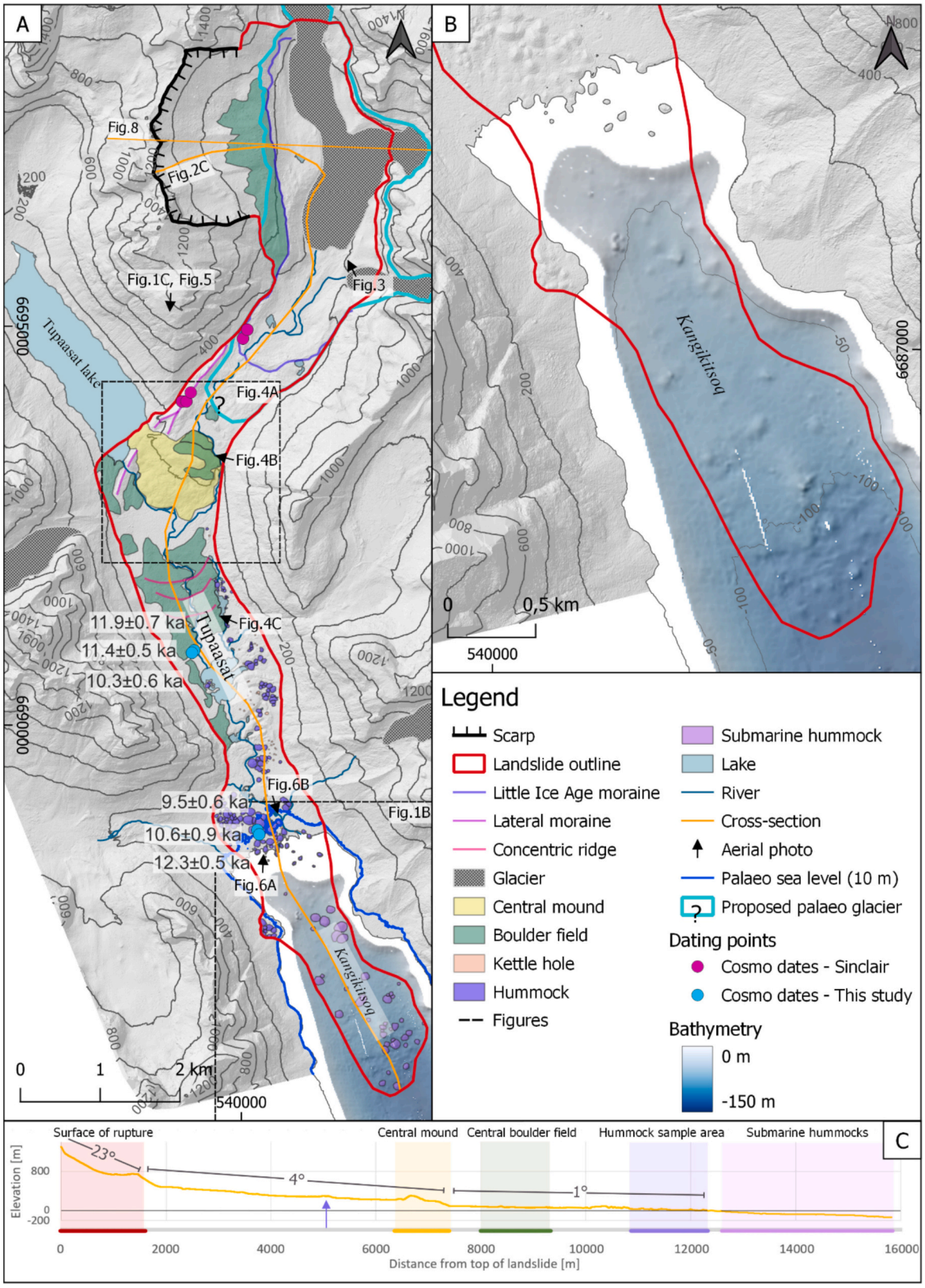

Fig. 2. A) Geomorphological map of the Tupaasat rock avalanche deposits within the landslide outline together with the paleo-sea level line at 10 m a.s.l., and the proposed paleo-ice sheet extent. The positions of the cross-sections depicted in Figs. 2C and 8 are shown as orange lines. The arrows indicate the direction in which the aerial photos in the figures are taken, with numbers referring to the figure they are depicted. B) Map showing the bathymetry data and the landslide outline. The bathymetry data is acquired from the Danish Geodata Agency and is not suitable for navigation (© Geodatastyrelsen – GST-320-3378). The mapped hummocks can be seen onshore and offshore as positive features in the landscape C) Cross-section of Tupaasat rock avalanche with columns indicating the geomorphological features described in the results. The terrain slopes are presented below.

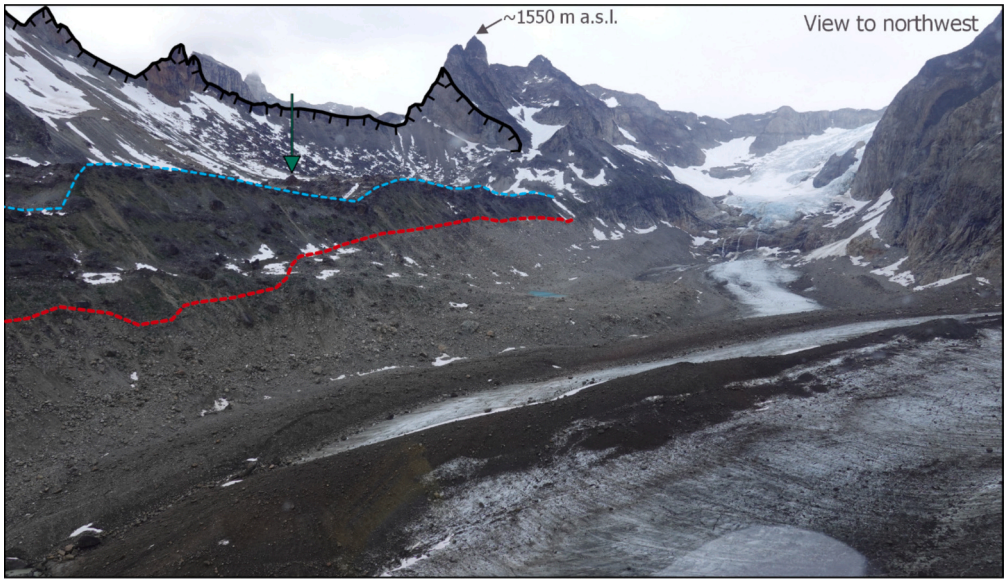

Fig. 3. Oblique aerial photo of the scarp area at the head of Tupaasat Valley looking northwest. The scar is marked with black, the hypothesized pre-slide glacier height is marked with a dashed blue line, and the glacier height during the LIA is marked with a dashed red line. Towards the west is the scarp area, with a green arrow pointing towards one of the boulders of c. 30 m in diameter, and at the valley floor, the present glacier is seen.

terminates the source area. On the eastern side of the ridge, we observe a change in colour from dark grey at the top to light grey below the line of change (Fig. 3, red line). The source volume is approximately 0.58 km^3. The scarp area has not been investigated in the field except for a pass with a helicopter. According to local 1:500,000 scale geological maps, the bedrock is composed of metagreywacke, metasiltstone, and metamudstone (Escher and Pulvertaft, 1995; Garde, 2007). However, this is not based on local field mapping but rather on interpretations of black and white aerial photos for regional-scale mapping. The basal surface of the scarp is now mostly covered by talus, and the lowermost part has been modified by glacial activity. The talus consists of boulders up to 30 m across on the slopes and in the lower part (Fig. 3). The slope of the failure area has an average steepness of 29°, while the slope along the cross-section in Fig. 2C is 23° steep.

4.1.2. *Central mound*

A large mound consisting of a diamict is located in the central part of the valley, where an abrupt change in slope from 4° to 1.5° occurs, 6.4 to 7.4 km from the scar (Fig. 2A, C). The mound is 1100 m wide and is up to 150 m higher than the surrounding valley floor (Fig. 4A, B). It occupies the whole width of the valley, and based on the contour lines, it has a slight fan shape down the valley. It is draped by large angular to

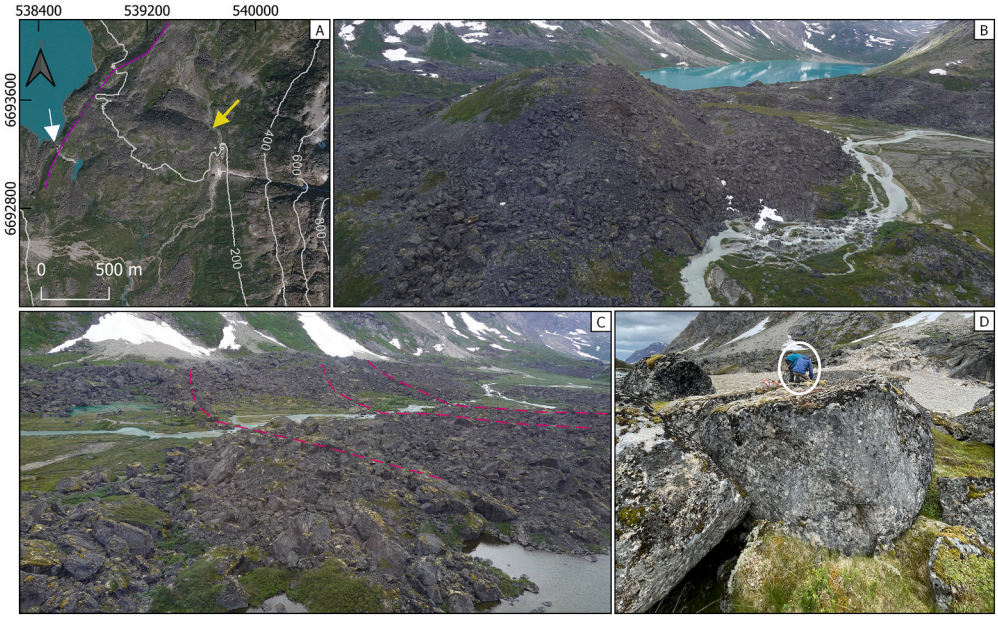

Fig. 4. Central mound and lateral moraine. A) Orthophoto of the central mound (yellow arrow). The central mound partially overlays the western moraine (dashed part of purple line), which has been incised by the lake upstream (white arrow), uncovering its interior. B) Oblique view of the central mound looking west-northwest. Boulders mantle its surface. Tupaasat Lake is seen in the background. C) Oblique view of the central boulder field looking northwest. The compressional ridges, marked with pink dashed lines, appear as spikes towards the meandering river at the center of the valley. D) Boulder sampling for dating, the two people used as scales are circled in white.

subangular boulders up to 30 m in diameter (Fig. 4B). There is a higher concentration of boulders in the northern part of the mound. Arctic vegetation covers the surface of the mound where there are no boulders. Based on this, the material under the vegetation must be fine-grained compared to the boulders, consisting of sand and gravel. The northwestern part of the mound covers a pre-existing lateral moraine that runs along the northwestern side of the valley (Figs. 2A, 4A). A stream from Tupaasat Lake erodes the lateral moraine exposing fine-grained, sandy to gravelly, light-yellow deposits of the moraine (Fig. 4A).

4.1.3. Central boulder field

A major boulder field is located 0.5 km down valley of the mound (Figs. 2A, 4C). The boulders are angular to subangular and up to 45 m across (Fig. 4C, D). Generally, the boulders are similar in size and shape to those observed in the rock avalanche scarp and on the central mound. Within the boulder field, we identify three concentric ridges crossing the valley 8.4 to 8.9 km from the scar (Figs. 2A, 5C). The three ridges are 8 to 15 m higher than the surrounding boulder field, and they consist of boulders at the crest and finer-grained debris in the lower part of the ridges, especially visible on the side facing south, down the valley. The finer-grained debris consists of smaller boulders and gravel at the axis of the valley, with an increasing content of gravel and sand towards the sides of the valley.

4.1.4. Outwash plain

At 10.0 to 10.9 km downslope of the scar, we observe a 0.47 km^2 area without major boulders and with a flat sloping surface (Figs. 2C, 5). The surface is sloping towards the axis of the valley by approximately 5°. The relatively smooth surface of the landform is incised by steep-sided, up to 35 m deep, V-shaped gullies and smaller circular depressions. It consists of a fine-grained deposit of sandy to gravelly-sized grains, with pebbles and smaller boulders draping some of the gullies. The circular depressions with a diameter between 5 and 45 m are mostly located in the northern part of the sloping outwash plain. Individual similar depressions are also observed inside the hummocks in the vicinity of the fjord (see Section 4.1.5).

4.1.5. Hummocks

At a distance of 10.9 to 12.3 km from the scar, 92 rock avalanche-generated hummocks are identified and measured (further details see Supplementary Information) (Fig. 2). The hummocks are very similar and generally have a cone-like morphology with a round to oval shape and a pointy summit (Fig. 6A). Most of the hummocks are covered with dense Arctic vegetation (Fig. 6B). In some cases, the surface deposits are exposed and reveal that the hummocks are generally composed of a diamict. Larger boulders, reaching up to 15 m in size, often drape the hummocks and create a rim at the periphery of the individual hummocks. Additionally, five circular depressions up to 30 m in diameter are mapped in the area of the hummocks (Fig. 6C).

The heights range from 0.5 to 36.5 m, and the hummocks are up to 140 m in diameter (Fig. 6D). For 63 % of these hummocks, the longest axis is oriented perpendicular to the runout direction. The slope along the axis parallel to the runout varies between 2.5° to 31.5°, while those on the axis perpendicular to the runout vary between 2° to 47.5°. The largest hummocks are at the center of the valley, whilst the smaller ones are predominantly located along the western flank. The hummocks do not diminish in size towards the end of the rock avalanche deposits (Figs. 2B, 6D).

On a small promontory on the western shore of the fjord, we identify 11 additional hummocks. On the bathymetry data, 42 submarine hummocks are mapped up to 15.8 km downslope of the scar on the seabed down to a depth of 120 m below sea level (Fig. 2A, B). They are of similar size and morphology to the onshore hummocks. Some uncertainty regarding the exact size of the submarine hummocks is expected due to the limitations of the resolution of the bathymetry data. Finally, 7 hummocks are observed as small islets up to 68 m across in the present-day coastal zone. Overall, all the hummocks in the distal part of the rock-avalanche deposits are of similar size and morphology (Figs. 2B, 6D).

4.2. ^{10}Be exposure dating

The measured ^{10}Be concentrations in the three boulders sampled from the top of two hummocks result in apparent exposure ages of 9.5 ± 0.6 ka (GL2204), 10.6 ± 0.9 ka (GL2205) and 12.3 ± 0.5 ka (GL2206), all including internal uncertainties. The measured ^{10}Be concentrations

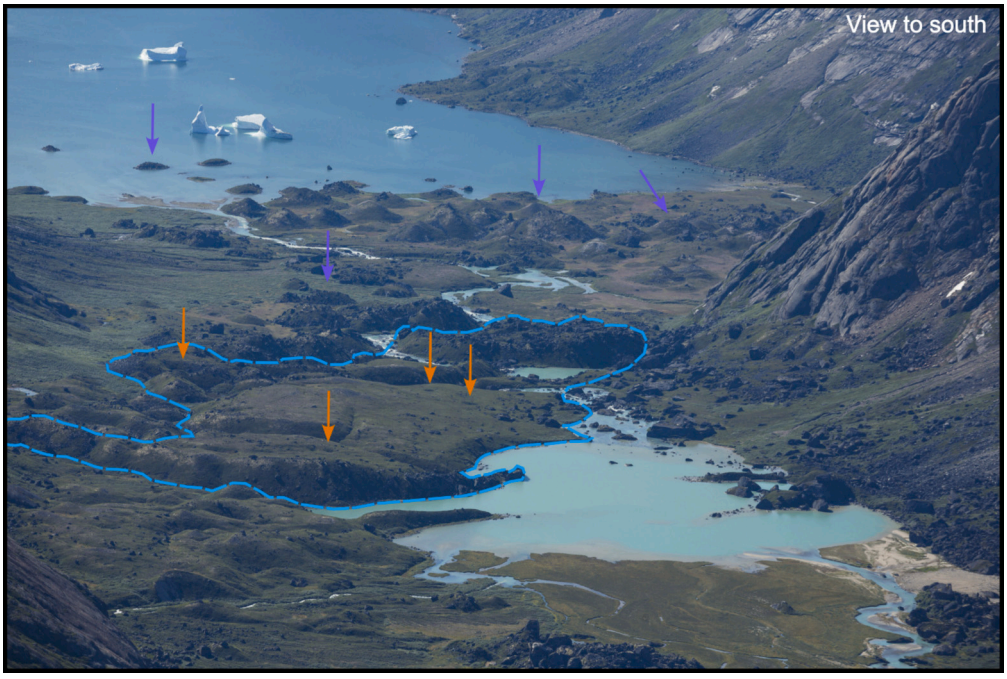

Fig. 5. Outwash plain. The orange arrows point to the locations of some of the kettle holes. Outwash plain is highlighted with the blue dashed line. The purple arrows point to the location of some of the hummocks, showing the extent of these.

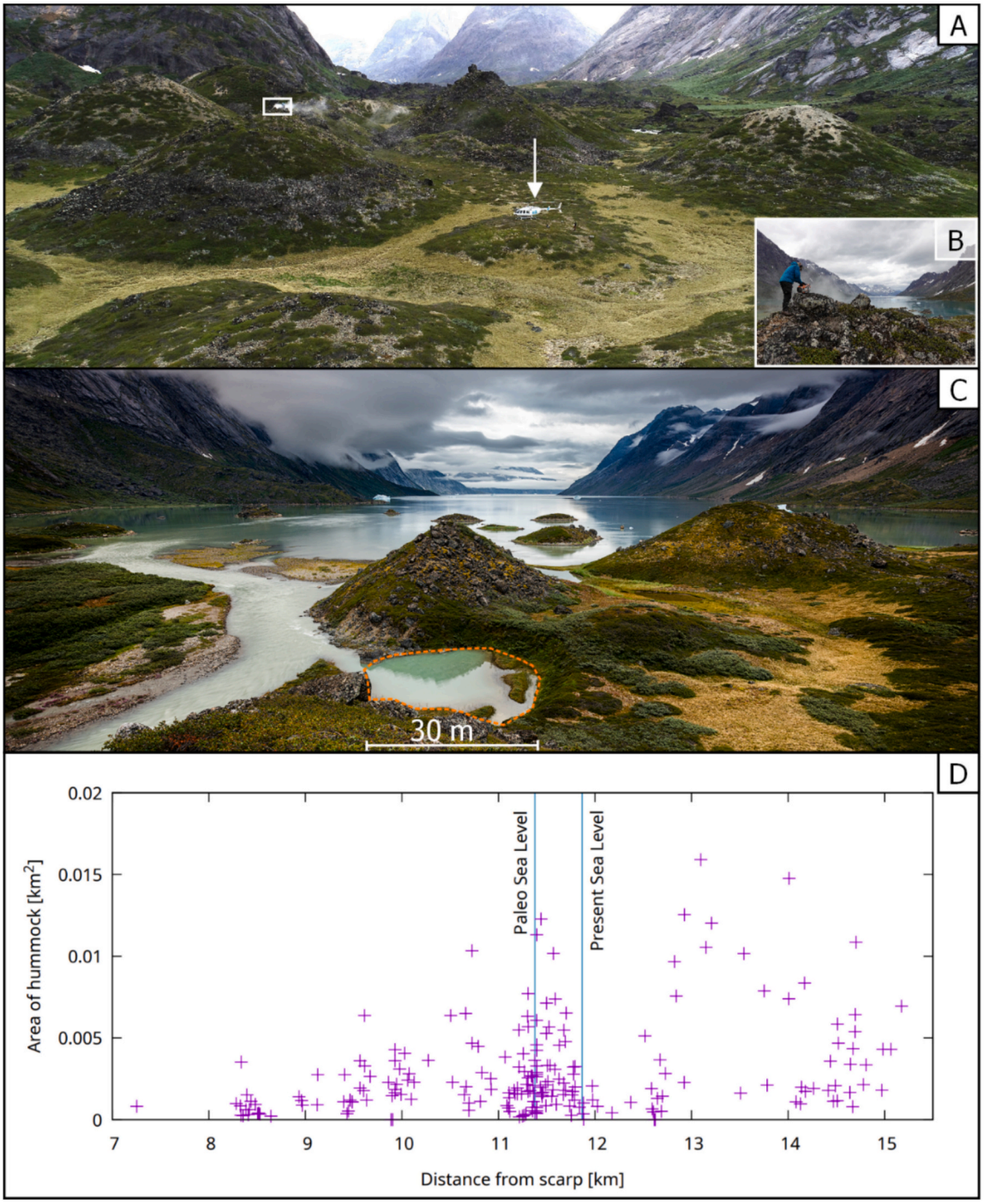

Fig. 6. Hummocks at the mouth of Tupaasat Valley. A) Field photo of hummocks, view towards north. The white arrow indicates the helicopter, and the white square indicates the location of the boulders sampled for cosmogenic nuclide exposure dating. B) View towards the south of boulders on a hummock sampled for cosmogenic nuclide exposure dating. C) View of hummocks looking south. The orange dashed line highlights a kettle hole with a width of 30 m (Photo: Urs Zihlmann). D) Graph of hummock size distribution showing the area of the hummocks mapped down through the valley. The blue column shows the present-day sea level, and the green column shows the paleo sea level, which was 10 m above the present.

in the three large boulders sampled in the boulder field result in apparent exposure ages of 11.9 ± 0.7 ka (GL2207), 11.4 ± 0.5 ka (GL2208) and 10.3 ± 0.6 ka (GL2209), all including internal uncertainties. A total weighted mean fulfilling the chi-square test for all six samples results in an age of 10.9 ± 0.5 ka using external uncertainties. Age distributions for all six boulders span c. 14 to 8 ka (Fig. 7), with a summed probability peak from c. 12.5 ka to 10 ka. All ages and additional sample information can be found in Table 1.

5. Discussion

5.1. Rock avalanche-related landforms

Based on our observations, we interpret the described geomorphological features seen in the Tupaasat Valley as rock-avalanche landforms, which we will discuss in the following sections.

We interpret the talus and boulders deposited at the lower part along the ridge of the c. 2.7 km^2 large source area as rock avalanche deposits.

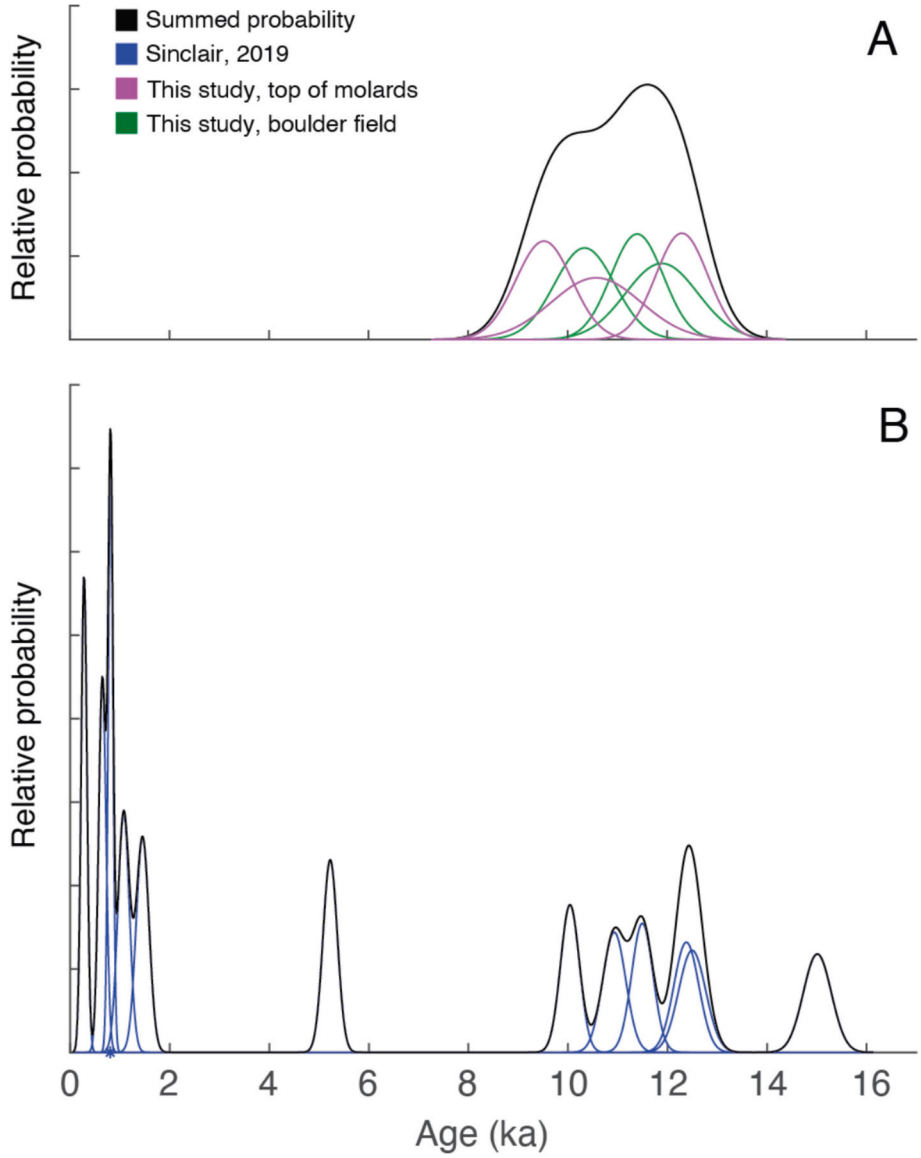

Fig. 7. Normal kernel density estimates of ^{10}Be exposure ages from the Tupaasat Valley (for location see Fig. 3). A) shows ^{10}Be ages including internal uncertainties from boulder samples in the central boulder field and on top of a molard sampled in this study. Mean for the six boulder samples, including external uncertainties, is 10.9 ± 0.5 ka. B) shows ^{10}Be ages from the late glacial and LIA moraines farther up the valley close to the present ice margin (Sinclair, 2019).

The talus in the source area on the slope from the mountain crest to around 750 m a.s.l. we interpret as talus from slope failures occurring after the rock avalanche.

We interpret the central mound (Section 4.1.2) as displaced material from the failure scar deposited during the later stages of the rock avalanche. This is based on how the central mound covers some part of the lateral moraine, together with the composition of sandy to gravelly material, with boulders similar to those observed at the bottom of the failure scar. The accumulation of boulders in the northern part of the mound could be caused by outwash of sand and gravel by meltwater from the LIA glacier retreat. Similar mounds, concluded to be landslide deposits, have been described in the periglacial area on the east side of Mount Shiroumadake in Japan (Kariya et al., 2011). Since the mound partially overlays the lateral moraine, it suggests that the lateral moraine predates the failure event and that the moraine might have been modified by the rock avalanche.

We interpret the central boulder field lying 0.5 km downslope from the central mound (Section 4.1.3) as a part of the rock avalanche, based on the size and similarities to the boulders seen in the lower part of the source area. Similar block fields are a very characteristic feature of rock avalanches and have been observed in many places (Hermanns et al., 2021). The concentric ridges observed in this boulder field are enigmatic. We speculate that they could have formed as compressional ridges from emplacement of the central mound, where the slope angle changes from c. 4° to 1.5°, provided the mound was deposited during the later stages of the rock avalanche. Nevertheless, these relationships remain challenging to conclusively establish.

The smooth-sloping, fine-grained plain observed 10 to 10.9 km downslope of the scar (Section 4.1.4) is interpreted to be an outwash plain that pre-existed the rock avalanche and was modified by it. However, as we lack field evidence from the outwash plain, this is difficult to verify how exactly it has been modified, except from the observations of it sloping towards the center of the valley and from the rock avalanche-generated hummocks and circular depressions observed around and on top of it. The V-shaped gullies are interpreted as erosional gullies, indicating a phase of water escape from the surface, while the circular depressions are interpreted as kettle holes formed by the melting of glacier ice. These kettle holes are also observed farther down-

valley, where the hummocks are located.

We interpret the hummocks in the distal part of the valley as molards deposited by the rock avalanche as ice-cemented blocks (c.f. Morino et al., 2019, 2023; Svennevig et al., 2023). Molards are landforms seen in landslide deposits in permafrozen environments. They are collapsed structures, deposited as ice-cemented blocks, and as the ice in the blocks thaws over time, they are left as conical mounds in the landscape. From the remote-sensing analysis, we see that they are larger in size but similar in shape to previously studied molards (c.f. Morino et al., 2019, 2023). Yoshida et al. (2012) show that hummocks diminish in size with runout, which is not observed in this study (Fig. 6D). As molards frequently occur in areas subject to glacial debuttressing we hypothesise that the conical mounds are molards (Yoshida et al., 2012; Paguican et al., 2014; Dufresne and Geertsema, 2020). However, while these characteristics strongly support our interpretation, a conclusive determination of the nature and origin of the cone-shaped features would require field investigation, as we also can't say for certain where the material for the molards originates from. We hypothesise that the impact of the rock avalanche led to mechanical permafrost degradation of glacial sediment located in front of the past glacier tongue and entrained the ice-cemented blocks of sediment into the rock avalanche, transporting them to the distal part of the deposit. Molards are also known from Central West Greenland (Svennevig et al., 2022, 2023). However, they are not as large as the ones seen in Tupaasat Valley, and they are distributed throughout the deposit. The Central West Greenland landslides are exclusively frozen debris avalanches and do not have a bedrock fraction as seen in the deposits from the Tupaasat rock avalanche.

Based on the islands at the head of the fjord, the 11 molards mapped on the western bank 0.7 m from the head of the fjord, and the molards mapped on the bathymetric data, we conclude that the ice-cemented blocks ran out into the fjord, forming submarine molards. We use this to define the toe of the rock avalanche deposit as the southernmost occurrence of submarine molards (Fig. 2B).

The presence of kettle holes throughout the lower half of the onshore rock avalanche deposit indicates that a significant portion of the rock avalanche could have encompassed massive ice, presumably of glacial origin.

In summary, the geomorphological mapping has allowed us to identify the segregation of the displaced material from the Tupaasat rock avalanche throughout the deposit, which, from proximal to distal, is distinguished into a large mound, a boulder field, and finally molards and kettle holes. The rock avalanche event thus probably encompassed both bedrock material (the large mound and the boulder fields), entrained permafrozen glaciogenic sediment (the molards) and glacial ice (kettle holes). This entrained material is possibly sourced from the area around 250 m elevation below the scarp, which today is occupied by glacier ice and moraine material (Fig. 2A).

The volume of the scar is 0.58 km^3 assuming a simple pre-slide geometry topography. To reconstruct the total volume of the rock avalanche deposit, bulking of the rock, due to fracturing during transportation which usually adds 25 % to the volume (Hungr and Evans, 2004), the deposit still inside the scar, and the entrainment of the glacier ice and the permafrozen sediments has to be added. By area, the molard fields, representing the entrained material, account for half of the deposit (Fig. 2A, B). The true total volume of the rock avalanche deposit is thus probably more than 1 km^3. This classifies the rock avalanche as a giant event (McColl and Cook, 2024).

5.2. The emplacement of the rock avalanche and its temporal relation to the deglaciation history

A weighted mean for the six boulders we sampled for ^{10}Be exposure dating, three on top of one hummock and three in the central boulder field, suggests that the rock avalanche was emplaced around 10.9 ± 0.5 ka (Table 1, Fig. 8) but with a full age span from 12.3 ± 0.5 to 9.5 ± 0.6 ka. The overlap between individual ages from the two landforms suggests that they most likely were formed in one event, as also indicated by the segregation of the rock avalanche deposit. As part of the rock avalanche deposits (the mound) is superimposed on the lateral moraine, it must be similar in age or younger than the moraine, which has been dated to c. 12.5 to 10 ka (Sinclair, 2019) (Fig. 7). Accordingly, we believe that the rock avalanche occurred shortly after the deglaciation of the area at the onset of the Holocene. At this time, the ice margin was either located in the upper part of the valley or further down close to the moraine and was disintegrated upon impact of the rock avalanche (Figs. 2A, 8).

5.3. Preconditioning factors and the tsunamigenic potential of the rock avalanche

As mentioned above, the timing of deglaciation and rock avalanche overlap in time (Fig. 7), and this leads us to suggest that glacial debuttressing of the slope destabilized the mountain slope (Dai et al., 2020; Kos et al., 2016).

Earthquakes may potentially trigger rock avalanches (Eaves et al., 2023); however, southern Greenland is at present a tectonically quiet area with few and small earthquakes (Voss et al., 2007). At 10.6 ka, during the deglaciation of the GrIS, a glacially triggered earthquake offshore in southern Greenland has been proposed (Steffen et al., 2020) and triggering by earthquakes cannot be ruled out. We emphasize the setting of the source area with a glacier immediately below the source area and suggest glacial debuttressing as a central preconditioning factor leading to the failure event, while the earthquake could have played a role as a final triggering event for the Tupaasat rock avalanche. Thermal permafrost degradation in mountainous periglacial areas can

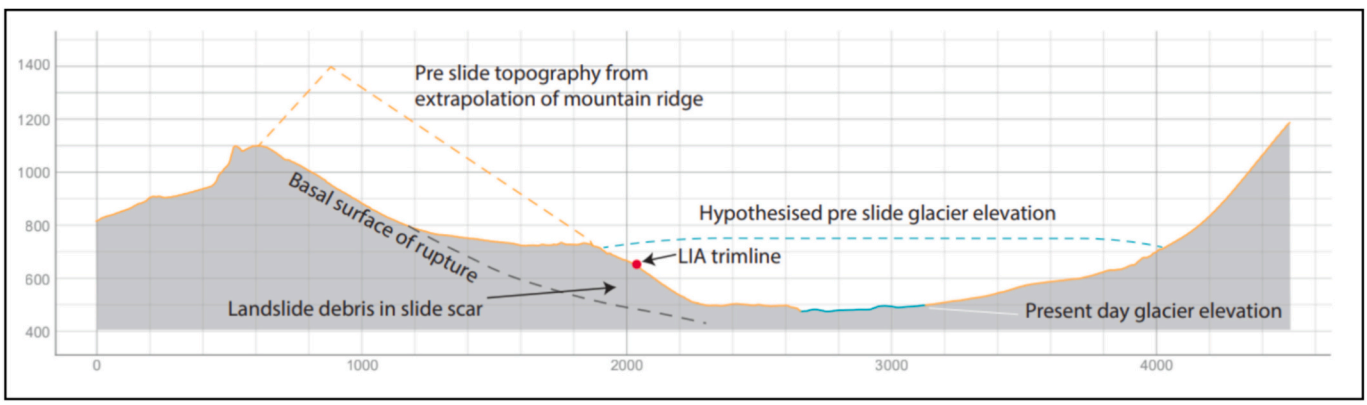

Fig. 8. Cross-section of the source area and the head of Tupaasat Valley with the estimated past mountain ridge and glacier elevation depicted. Axis are in meters.

also lead to an increased risk of landslides (Coe et al., 2018; Tapia Baldis and Trombotto Liaudat, 2019), but it most likely did not act as a preconditioning or triggering factor for the Tupaasat rock avalanche. We believe that the molards were formed from the impact of the Tupaasat rock avalanche into permafrozen glacial sediments, leading to mechanical permafrost degradation. A similar process has been proposed for large molards on Mars (Morino et al., 2023).

We suggest that the rock avalanche impacted the glacier and associated frozen glacial sediments entraining glacier ice and ground-ice rich material on its way down the Tupaasat Valley. This led to reduced friction (Hungr and Evans, 2004), and the rock mass gained higher velocities (Bessette-Kirton and Coe, 2020; Deline, 2009; Reznichenko et al., 2011). This resulted in a very mobile rock avalanche as also shown by the low fahrböschung. The rockslide thus most probably transformed into a rock-ice avalanche as indicated by the presence of kettle holes in the deposit potentially representing glacier ice caught in the deposit. The boulders in the central boulder field were the first ones to be deposited. This was followed by the deposition of ice blocks and the permafrozen blocks farther into the fjord. The ice blocks and the permafrozen blocks thawed over time and respectively shaped the kettle holes and molards seen in the landscape today. The presence of molards in the rock-ice avalanche deposit suggests the presence of permafrost at high elevations below the source area which is not surprising given the high elevation and glacial conditions there. Fluid resulting from the thawing of ground ice may have further increased the runout and destructiveness of the Tupaasat rock-ice avalanche (Allstadt et al., 2024; Brideau et al., 2019; Morino et al., 2023, 2021).

The Tupaasat rock-ice avalanche was very mobile (fahrböschung of 0.09), implying high emplacement energy, and a significant (yet unconstrained) volume of the rock-ice avalanche, with entrained material mainly consisting of glacier ice and blocks of frozen rocks and sediments. It would have impacted the sea and we suggest that it could have created a significant tsunami. In future studies, the generating of tsunami models or the search for tsunami deposits in isostatic raised lakes around the Kangikitsoq Fjord could significantly enhance the understanding of the impacts caused by the Tupaasat rock-ice avalanche (Korsgaard et al., 2024). The tsunamigenic potential of frozen debris avalanches consisting of such permafrost deposits has been demonstrated for three historic events (1952, 1996 and 2000 CE) in Vaigat Strait, Central West Greenland (Dahl-Jensen et al., 2004; Svennevig et al., 2023, 2025). The Tupaasat rock-ice avalanche serves as a potential scenario for present-day glacial and periglacial fjords, in which climate change increases the likelihood of tsunamigenic landslides occurring. Such events have recently been described from East Greenland (Svennevig et al., 2024a), highlighting the urgency of gaining a better understanding of these events for assessing future risk in inhabited fjord areas.

6. Conclusion

The large Tupaasat rock-ice avalanche, with a runout length of approximately 15.8 km, fahrböschung of 0.09, and a total volume potentially exceeding 1 km^3, including the entrainment of material, produced a set of landforms including a large mound, a boulder field, kettle holes, and molards. The landforms have been dated using ^{10}Be exposure dating, resulting in an age range from 12.3 ± 0.5 to 9.5 ± 0.6 ka with a weighted mean age of 10.9 ± 0.5 ka. This indicates a possible link between the failure event and the deglaciation of the valley. Accordingly, we find it likely that the initial rockslide was preconditioned by glacial debuttressing associated with glacial thinning, while mechanical permafrost degradation and the presence of ice determined the size of the rock-ice avalanche. The Tupaasat rock-ice avalanche was very likely tsunamigenic, as indicated by the molards found in the fjord and the high mobility of the event. With the potential for increased glacial thinning in the near future, the risk of rock-ice avalanches of similar magnitude could rise. As seen in the deposits of the Tupaasat rock-ice avalanche, these large-scale landslides can be destructive and potentially fatal if they occur in inhabited areas. Thus, it is critical to consider these factors when conducting risk assessments for populations living near glaciated valleys and fjords to mitigate the impact a potential failure could have.

CRediT authorship contribution statement

L.L. Pedersen: Writing – original draft, Visualization, Project administration, Investigation, Formal analysis, Data curation. **K. Svennevig:** Writing – review & editing, Writing – original draft, Supervision, Resources, Investigation, Conceptualization. **C. Morino:** Writing – review & editing, Supervision, Investigation. **A.S. Søndergaard:** Writing – review & editing, Writing – original draft, Resources, Investigation. **C. Pearce:** Writing – review & editing, Supervision. **L.F. Pérez:** Writing – review & editing, Supervision, Data curation. **A. Damsgaard:** Writing – review & editing. **J. Olsen:** Formal analysis. **M.F. Knudsen:** Formal analysis. **A. Noblet:** Data curation. **N.K. Larsen:** Writing – review & editing, Writing – original draft, Supervision, Resources, Investigation, Conceptualization.

Declaration of competing interest

The author declares no conflict of interest.

Acknowledgements

Permission to use the bathymetry data collected in the area by the Danish Geodata Agency was granted by © Geodatastyrelsen – GST-320-3378. We thank Tilmann Graner and Urs Zihlmann for the use of their photos from their journeys in Tupaasat Valley.

This project received funding from Independent Research Fund Denmark (case number: 1025-00007B), the Swiss Polar Institute and BNP Paribas Swiss Foundation (grant number PAF-2022-004), Geocenter Danmark project: Landslides in a changing climate, the RETURN Extended Partnership-European Union Next-GenerationEU (National Recovery and Resilience Plan – NRRP, Mission 4, Component 2, Investment 1.3 – D.D. 1243 2/8/2022, PE0000005). NKL acknowledge support from the Novo Nordisk Foundation under the Challenge Programme 2023 - Grant number NNF23OC00807040 and the Villum Foundation (project no. 40816). AN was funded by the Agence Nationale de la Recherche in the framework of the project ANR-19-CE01-0010 PERMOLARDS.

Appendix A. Supplementary data

Supplementary data to this article can be found online at https://doi.org/10.1016/j.geomorph.2025.110057.

Data availability

Data will be made available on request.

References

Agency for Climate Data, n.d. Højdemodel Grønland [WWW Document]. URL https://dataforsyningen.dk/ (accessed 11.17.24).

Allstadt, K.E., Coe, J.A., Collins, E.A., Rengers, F.K., Mangeney, A., Esser, S.M., Pursley, J., Yeck, W.L., Bellini, J.J., Brady, L.R., 2024. The 2022 Chaos Canyon landslide in Colorado: insights revealed by seismic analysis, field investigations, and remote sensing. Landslides 21, 309–325. https://doi.org/10.1007/s10346-023-02179-4.

Andersen, J.L., Egholm, D.L., Olsen, J., Larsen, N.K., Knudsen, M.F., 2020. Topographical evolution and glaciation history of South Greenland constrained by paired $^{26}Al/^{10}Be$ nuclides. Earth Planet. Sci. Lett. 542. https://doi.org/10.1016/j.epsl.2020.116300.

Balco, G., Stone, J.O., Lifton, N.A., Dunai, T.J., 2008. A complete and easily accessible means of calculating surface exposure ages or erosion rates from 10Be and 26Al measurements. Quat. Geochronol. 3, 174–195. https://doi.org/10.1016/j.

quageo.2007.12.001. Prospects for the New Frontiers of earth and Environmental Sciences.
Ballantyne, C.K., 2002. Paraglacial geomorphology. Quat. Sci. Rev. 21, 1935–2017. https://doi.org/10.1016/S0277-3791(02)00005-7.
Bennike, O., Björck, S., 2002. Chronology of the last recession of the Greenland Ice Sheet. J. Quat. Sci. 17, 211–219. https://doi.org/10.1002/jqs.670.
Bessette-Kirton, E.K., Coe, J.A., 2020. A 36-year record of rock avalanches in the Saint Elias Mountains of Alaska, with implications for future hazards. Front. Earth Sci. 8. https://doi.org/10.3389/feart.2020.00293.
Bøgvad, R., 1940. Quaternary geological observations etc. in South-East and South Greenland. Medd. Grønland 107 (3), 1–42.
Borgatti, L., Soldati, M., 2010. Landslides as a geomorphological proxy for climate change: a record from the Dolomites (northern Italy). Geomorphology 120, 56–64. https://doi.org/10.1016/j.geomorph.2009.09.015. Landslide geomorphology in a changing environment.
Brideau, M.-A., Shugar, D.H., Bevington, A.R., Willis, M.J., Wong, C., 2019. Evolution of the 2014 Vulcan Creek landslide-dammed lake, Yukon, Canada, using field and remote survey techniques. Landslides 16, 1823–1840. https://doi.org/10.1007/s10346-019-01199-3.
Carlson, A., Stoner, J., Donnelly, J., Hillarie-Marcel, C., 2008. Response of the southern Greenland Ice Sheet during the last two deglaciations. Geology 36 (5), 359–362.
Cathala, M., Bock, J., Magnin, F., Ravanel, L., Ben Asher, M., Astrade, L., Bodin, X., Chambon, G., Deline, P., Faug, T., Genuite, K., Jaillet, S., Josnin, J.-Y., Revil, A., Richard, J., 2024. Predisposing, triggering and runout processes at a permafrost-affected rock avalanche site in the French Alps (Étache, June 2020). Earth Surf. Process. Landf. 49, 3221–3247. https://doi.org/10.1002/esp.5881.
Coe, J.A., Bessette-Kirton, E.K., Geertsema, M., 2018. Increasing rock-avalanche size and mobility in Glacier Bay National Park and Preserve, Alaska detected from 1984 to 2016 Landsat imagery. Landslides 15, 393–407. https://doi.org/10.1007/s10346-017-0879-7.
Cook, S.J., Porter, P.R., Bendall, C.A., 2013. Geomorphological consequences of a glacier advance across a paraglacial rock avalanche deposit. Geomorphology 189, 109–120. https://doi.org/10.1016/j.geomorph.2013.01.022.
Corbett, L.B., Bierman, P.R., Rood, D.H., 2016. An approach for optimizing *in situ* cosmogenic ^{10}Be sample preparation. Quat. Geochronol. 33, 24–34. https://doi.org/10.1016/j.quageo.2016.02.001.
Cossart, E., Braucher, R., Fort, M., Bourlès, D.L., Carcaillet, J., 2008. Slope instability in relation to glacial debuttressing in alpine areas (Upper Durance catchment, southeastern France): evidence from field data and ^{10}Be cosmic ray exposure ages. Geomorphology 95, 3–26. https://doi.org/10.1016/j.geomorph.2006.12.022. Paraglacial Geomorphology: Processes and Paraglacial Context.
Dahl-Jensen, T., Larsen, L.M., Pedersen, S.A.S., Pedersen, J., Jepsen, H.F., Pedersen, G., Nielsen, T., Pedersen, A.K., Von Platen-Hallermund, F., Weng, W., 2004. Landslide and tsunami 21 November 2000 in Paatuut, West Greenland. Nat. Hazards 31, 277–287. https://doi.org/10.1023/B:NHAZ.0000020264.70048.95.
Dai, C., Higman, B., Lynett, P.J., Jacquemart, M., Howat, I.M., Liljedahl, A.K., Dufresne, A., Freymueller, J.T., Geertsema, M., Ward Jones, M., Haeussler, P.J., 2020. Detection and assessment of a large and potentially tsunamigenic periglacial landslide in Barry Arm, Alaska. Geophys. Res. Lett. 47, e2020GL089800. https://doi.org/10.1029/2020GL089800.
Deline, P., 2009. Interactions between rock avalanches and glaciers in the Mont Blanc massif during the late Holocene. Quat. Sci. Rev. 28, 1070–1083. https://doi.org/10.1016/j.quascirev.2008.09.025. Natural Hazards, Extreme Events and Mountain Topography.
Dufresne, A., Geertsema, M., 2020. Rock slide–debris avalanches: flow transformation and hummock formation, examples from British Columbia. Landslides 17, 15–32. https://doi.org/10.1007/s10346-019-01280-x.
Eaves, S.R., McColl, S.T., Tielidze, L.G., Norton, K.P., Hopkins, J.L., Hidy, A.J., 2023. The age and potential causes of the giant Green Lake Landslide, Fiordland, New Zealand. Landslides 20, 1883–1892. https://doi.org/10.1007/s10346-023-02075-x.
Escher, Jan C., Pulvertaft, T. Christopher R., 1995. Geological map of Greenland 1:2 500 000. https://doi.org/10.22008/FK2/SYAL4J.
Fey, C., Wichmann, V., Zangerl, C., 2017. Reconstructing the evolution of a deep seated rockslide (Marzell) and its response to glacial retreat based on historic and remote sensing data. Geomorphology 298, 72–85. https://doi.org/10.1016/j.geomorph.2017.09.025.
Funder, S., Kjeldsen, K.K., Kjær, K.H., Cofaigh, C.Ó., 2011. The Greenland Ice Sheet during the past 300,000 years: a review. In: Quaternary Glaciations - Extent and Chronology: a Closer Look. Elsevier, pp. 699–713. https://doi.org/10.1016/B978-0-444-53447-7.00050-7.
Garde, Adam A., 2007. Geological map of Greenland, 1:500 000, Sheet 1, Sydgrønland, 2nd edition. https://doi.org/10.22008/FK2/L4LGK6.
Grämiger, L.M., Moore, J.R., Gischig, V.S., Ivy-Ochs, S., Loew, S., 2017. Beyond debuttressing: mechanics of paraglacial rock slope damage during repeat glacial cycles. J. Geophys. Res. Earth 122, 1004–1036. https://doi.org/10.1002/2016JF003967.
Hermanns, R., Penna, I., Oppikofer, T., Noël, F., Velardi, G., 2021. Rock Avalanche. In: Reference Module in Earth Systems and Environmental Sciences. https://doi.org/10.1016/B978-0-12-818234-5.00183-8.
Hermanns, R.L., L'Heureux, J.S., Blikra, L.H., 2013. Landslide Triggered Tsunami, Displacement Wave. In: Bobrowsky, P.T. (Ed.), Encyclopedia of Natural Hazards, Encyclopedia of Earth Sciences Series. Springer, Dordrecht. https://doi.org/10.1007/978-1-4020-4399-4_95.
Hungr, O., Evans, S.G., 2004. Entrainment of debris in rock avalanches: an analysis of a long run-out mechanism. GSA Bull. 116, 1240–1252. https://doi.org/10.1130/B25362.1.
Hungr, O., Leroueil, S., Picarelli, L., 2014. The Varnes classification of landslide types, an update. Landslides 11, 167–194. https://doi.org/10.1007/s10346-013-0436-y.
Ivy-Ochs, S., Kober, F., 2008. Surface exposure dating with cosmogenic nuclides. E G Quat. Sci. J. 57, 179–209. https://doi.org/10.3285/eg.57.1-2.7.
Kaplan, M.R., Wolfe, A.P., Miller, G.H., 2002. Holocene environmental variability in southern Greenland inferred from lake sediments. Quatern. Res. 58, 149–159. https://doi.org/10.1006/qres.2002.2352.
Kariya, Y., Sato, G., Komori, J., 2011. Landslide-induced terminal moraine-like landforms on the east side of Mount Shiroumadake, Northern Japanese Alps. Geomorphology 127, 156–165. https://doi.org/10.1016/j.geomorph.2010.12.012.
Kjær, K.H., Bjørk, A.A., Kjeldsen, K.K., Hansen, E.S., Andresen, C.S., Siggaard-Andersen, M.-L., Khan, S.A., Søndergaard, A.S., Colgan, W., Schomacker, A., Woodroffe, S., Funder, S., Rouillard, A., Jensen, J.F., Larsen, N.K., 2022. Glacier response to the Little Ice Age during the Neoglacial cooling in Greenland. Earth-Sci. Rev. 227. https://doi.org/10.1016/j.earscirev.2022.103984.
Korsgaard, N.J., Svennevig, K., Søndergaard, A.S., Luetzenburg, G., Oksman, M., Larsen, N.K., 2024. Evidence of Middle Holocene landslide-generated tsunamis recorded in lake sediments from Saqqaq, West Greenland. Nat. Hazards Earth Syst. Sci. 24, 757–772. https://doi.org/10.5194/nhess-24-757-2024.
Kos, A., Amann, F., Strozzi, T., Delaloye, R., von Ruette, J., Springman, S., 2016. Contemporary glacier retreat triggers a rapid landslide response, Great Aletsch Glacier, Switzerland. Geophys. Res. Lett. 43, 12,466–12,474. https://doi.org/10.1002/2016GL071708.
Lal, D., 1991. Cosmic ray labeling of erosion surfaces: *in situ* nuclide production rates and erosion models. Earth Planet. Sci. Lett. 104, 424–439. https://doi.org/10.1016/0012-821X(91)90220-C.
Larocca, L.J., Axford, Y., Bjørk, A.A., Lasher, G.E., Brooks, J.P., 2020. Local glaciers record delayed peak Holocene warmth in South Greenland. Quat. Sci. Rev. 241. https://doi.org/10.1016/j.quascirev.2020.106421.
Larsen, N.K., Kjær, K.H., Olsen, J., Funder, S., Kjeldsen, K.K., Nørgaard-Pedersen, N., 2011. Restricted impact of Holocene climate variations on the southern Greenland Ice Sheet. Quat. Sci. Rev. 30, 3171–3180.
Larsen, N.K., Find, J., Kristensen, A., Bjork, A.A., Kjeldsen, K.K., Odgaard, B.V., Olsen, J., Kjaer, K.H., 2016. Holocene ice marginal fluctuations of the Qassimiut lobe in South Greenland. Sci. Rep. 6, 22362.
Larsen, N.K., Levy, L.B., Carlson, A.E., Buizert, C., Olsen, J., Strunk, A., Bjork, A.A., Skov, D.S., 2018. Instability of the Northeast Greenland Ice Stream over the last 45,000 years. Nat. Commun. 9, 1872. https://doi.org/10.1038/s41467-018-04312-7.
Levy, L.B., Larsen, N.K., Knudsen, M.F., Egholm, D.L., Bjork, A.A., Kjeldsen, K.K., Kelly, M.A., Howley, J.A., Olsen, J., Tikhomirov, D., Zimmerman, S.R.H., Kjaer, K.H., 2020. Multi-phased deglaciation of south and southeast Greenland controlled by climate and topographic setting. Quat. Sci. Rev. 242.
Matthew, M.C., Gosse, J.C., Hermanns, R.L., Normandeau, A., Tremblay, T., 2024. Rock avalanches in northeastern Baffin Island, Canada: understanding low occurrence amid high hazard potential. Landslides 21, 2307–2326. https://doi.org/10.1007/s10346-024-02315-8.
McColl, S.T., Cook, S.J., 2024. A universal size classification system for landslides. Landslides 21, 111–120. https://doi.org/10.1007/s10346-023-02131-6.
Morino, C., Conway, S.J., Sæmundsson, Þ., Helgason, J.K., Hillier, J., Butcher, F.E.G., Balme, M.R., Jordan, C., Argles, T., 2019. Molards as an indicator of permafrost degradation and landslide processes. Earth Planet. Sci. Lett. 516, 136–147. https://doi.org/10.1016/j.epsl.2019.03.040.
Morino, C., Conway, S.J., Balme, M.R., Helgason, J.K., Sæmundsson, Þ., Jordan, C., Hillier, J., Argles, T., 2021. The impact of ground-ice thaw on landslide geomorphology and dynamics: two case studies in northern Iceland. Landslides 18, 2785–2812. https://doi.org/10.1007/s10346-021-01661-1.
Morino, C., Conway, S., Philippe, M., Peignaux, C., Svennevig, K., Lucas, A., Noblet, A., Roberti, G., Butcher, F., Collins-May, J., 2023. Permafrost molards as an analogue for ejecta-ice interactions at Hale Crater, Mars. Icarus 391, 115363. https://doi.org/10.1016/j.icarus.2022.115363.
Morlighem, M., Williams, C.N., Rignot, E.J., An, L., Arndt, J.E., Bamber, J.L., Catania, G. A., Chauché, N., Dowdeswell, J.A., Dorschel, B., Fenty, I., Hogan, K., Howat, I.M., Hubbard, A.L., Jakobsson, M., Jordan, T.M., Kjeldsen, K.K., Millan, R., Mayer, L., Mouginot, J., Noël, B.P.Y., O'Cofaigh, C., Palmer, S.J., Rysgaard, S., Seroussi, H., Siegert, M.J., Slabon, P., Straneo, F., van den Broeke, M.R., Weinrebe, W., Wood, M., Zinglersen, K.B., 2021. IceBridge BedMachine Greenland, Version 4. https://doi.org/10.5067/VLJ5YXKCNGXO.
Nishiizumi, K., Imamura, M., Caffee, M.W., Southon, J.R., Finkel, R.C., McAninch, J., 2007. Absolute calibration of ^{10}Be AMS standards. Nucl. Inst. Methods Phys. Res. B 258, 403–413. https://doi.org/10.1016/j.nimb.2007.01.297.
Paguican, E.M., van Wyk de Vries, B., Lagmay, A.M., 2014. Hummocks: how they form and how they evolve in rockslide-debris avalanches. Landslides 11. https://doi.org/10.1007/s10346-012-0368-y.
Porter, C., Morin, P., Howat, I., Noh, M.-J., Bates, B., Peterman, K., Keesey, S., Schlenk, M., Gardiner, J., Tomko, K., Willis, M., Kelleher, C., Cloutier, M., Husby, E., Foga, S., Nakamura, H., Platson, M., Wethington, M., Williamson, C., Bauer, G., Enos, J., Arnold, G., Kramer, W., Becker, P., Doshi, A., D'Souza, C., Cummens, P., Laurier, F., Bojesen, M., 2022. ArcticDEM, Version 3. https://doi.org/10.7910/DVN/OHHUKH.
Reznichenko, N.V., Davies, T.R.H., Alexander, D.J., 2011. Effects of rock avalanches on glacier behaviour and moraine formation. Geomorphology 132, 327–338. https://doi.org/10.1016/j.geomorph.2011.05.019.
Saemundsson, P., Morino, C., Conway, S.J., 2022. Mass-movements in cold and polar climates. In: Reference Module in Earth Systems and Environmental Sciences. Elsevier. https://doi.org/10.1016/B978-0-12-818234-5.00117-6.

Scheidegger, A.E., 1973. On the prediction of the reach and velocity of catastrophic landslides. Rock Mech. 5, 231–236. https://doi.org/10.1007/BF01301796.
Shugar, D.H., Jacquemart, M., Shean, D., Bhushan, S., Upadhyay, K., Sattar, A., Schwanghart, W., McBride, S., de Vries, M.V.W., Mergili, M., Emmer, A., Deschamps-Berger, C., McDonnell, M., Bhambri, R., Allen, S., Berthier, E., Carrivick, J.L., Clague, J.J., Dokukin, M., Westoby, M.J., 2021. A massive rock and ice avalanche caused the 2021 disaster at Chamoli, Indian Himalaya. Science 373 (6552), 300–306. https://doi.org/10.1126/science.abh4455.
Sinclair, G., 2019. North Atlantic Climate and Cryosphere Variability Over the Past 20,000 Years (Doctoral Thesis (compilation)). College of Earth, Ocean, and Atmospheric Sciences, Oregon State University, Corvallis.
Sinclair, G., Carlson, A.E., Mix, A.C., Lecavalier, B.S., Milne, G., Mathias, A., Buizert, C., DeConto, R., 2016. Diachronous retreat of the Greenland ice sheet during the last deglaciation. Quat. Sci. Rev. 145, 243–258. https://doi.org/10.1016/j.quascirev.2016.05.040.
Sparrenbom, C., 2006. Constraining the Southern Part of the Greenland Ice Sheet since the Last Glacial Maximum from Relative Sea-Level Changes, Cosmogenic Dates and Glacial-Isostatic Adjustment Models (Doctoral Thesis (compilation)). Department of Geology, Lund University.
Sparrenbom, C.J., Bennike, O., Björck, S., Lambeck, K., 2006. Holocene relative sea-level changes in the Qaqortoq area, southern Greenland. Boreas 35, 171–187. https://doi.org/10.1111/j.1502-3885.2006.tb01148.x.
Sparrenbom, C.J., Bennike, O., Fredh, D., Randsalu-Wendrup, L., Zwartz, D., Ljung, K., Björck, S., Lambeck, K., 2013. Holocene relative sea-level changes in the inner Bredefjord area, southern Greenland. Quat. Sci. Rev. 69, 107–124. https://doi.org/10.1016/j.quascirev.2013.02.020.
Steffen, R., Steffen, H., Weiss, R., Lecavalier, B.S., Milne, G.A., Woodroffe, S.A., Bennike, O., 2020. Early Holocene Greenland-ice mass loss likely triggered earthquakes and tsunami. Earth Planet. Sci. Lett. 546, 116443. https://doi.org/10.1016/j.epsl.2020.116443.
Stone, J.O., 2000. Air pressure and cosmogenic isotope production. J. Geophys. Res. Solid Earth 105, 23753–23759. https://doi.org/10.1029/2000JB900181.
Svennevig, K., 2019. Preliminary landslide mapping in Greenland. GEUS Bull. 43. https://doi.org/10.34194/GEUSB-201943-02-07.
Svennevig, K., Dahl-Jensen, T., Keiding, M., Merryman Boncori, J.P., Larsen, T.B., Salehi, S., Munck Solgaard, A., Voss, P.H., 2020. Evolution of events before and after the 17 June 2017 rock avalanche at Karrat Fjord, West Greenland – a multidisciplinary approach to detecting and locating unstable rock slopes in a remote Arctic area. Earth Surf. Dyn. 8, 1021–1038. https://doi.org/10.5194/esurf-8-1021-2020.
Svennevig, K., Hermanns, R.L., Keiding, M., Binder, D., Citterio, M., Dahl-Jensen, T., Mertl, S., Sørensen, E.V., Voss, P.H., 2022. A large frozen debris avalanche entraining warming permafrost ground—the June 2021 Assapaat landslide, West Greenland. Landslides 19, 2549–2567. https://doi.org/10.1007/s10346-022-01922-7.
Svennevig, K., Keiding, M., Korsgaard, N.J., Lucas, A., Owen, M., Poulsen, M.D., Priebe, J., Sørensen, E.V., Morino, C., 2023. Uncovering a 70-year-old permafrost degradation induced disaster in the Arctic, the 1952 Niiortuut landslide-tsunami in central West Greenland. Sci. Total Environ. 859, 160110. https://doi.org/10.1016/j.scitotenv.2022.160110.
Svennevig, K., Hicks, S.P., Forbriger, T., Lecocq, T., Widmer-Schnidrig, R., Mangeney, A., Hibert, C., Korsgaard, N.J., Lucas, A., Satriano, C., Anthony, R.E., Mordret, A., Schippkus, S., Rysgaard, S., Boone, W., Gibbons, S.J., Cook, K.L., Glimsdal, S., Løvholt, F., Van Noten, K., Assink, J.D., Marboeuf, A., Lomax, A., Vanneste, K., Taira, T., Spagnolo, M., De Plaen, R., Koelemeijer, P., Ebeling, C., Cannata, A., Harcourt, W.D., Cornwell, D.G., Caudron, C., Poli, P., Bernard, P., Larose, E., Stutzmann, E., Voss, P.H., Lund, B., Cannavo, F., Castro-Díaz, M.J., Chaves, E., Dahl-Jensen, T., Pinho Dias, N.D., Déprez, A., Develter, R., Dreger, D., Evers, L.G., Fernández-Nieto, E.D., Ferreira, A.M.G., Funning, G., Gabriel, A.-A., Hendrickx, M., Kafka, A.L., Keiding, M., Kerby, J., Khan, S.A., Dideriksen, A.K., Lamb, O.D., Larsen, T.B., Lipovsky, B., Magdalena, I., Malet, J.-P., Myrup, M., Rivera, L., Ruiz-Castillo, E., Wetter, S., Wirtz, B., 2024a. A rockslide-generated tsunami in a Greenland fjord rang Earth for 9 days. Science 385, 1196–1205. https://doi.org/10.1126/science.adm9247.
Svennevig, K., Owen, M.J., Citterio, M., Nielsen, T., Rosing, S., Harff, J., Endler, R., Morlighem, M., Rignot, E., 2024b. Holocene gigascale rock avalanches in Vaigat strait, West Greenland—Implications for geohazard. Geology 52, 147–152. https://doi.org/10.1130/G51234.1.
Svennevig, K., Keiding, M., Sørensen, E.V., Løvholt, F., Glimsdal, S., Perez, L.F., Owen, M. J., Morino, C., 2025. Two similar permafrost degradation landslides at Paatuut, West Greenland, caused tsunamis of substantially different magnitudes. Landslides 22, 1455–1474. https://doi.org/10.1007/s10346-024-02439-x.
Tapia Baldis, C., Trombotto Liaudat, D., 2019. Rockslides and rock avalanches in the Central Andes of Argentina and their possible association with permafrost degradation. Permafr. Periglac. Process. 30, 330–347. https://doi.org/10.1002/ppp.2024.
Voss, P., Poulsen, S.K., Simonsen, S.B., Gregersen, S., 2007. Seismic hazard assessment of Greenland. GEUS Bull. 13, 57–60. https://doi.org/10.34194/geusb.v13.4976.
Walter, F., Amann, F., Kos, A., Kenner, R., Phillips, M., de Preux, A., Huss, M., Tognacca, C., Clinton, J., Diehl, T., Bonanomi, Y., 2020. Direct observations of a three million cubic meter rock-slope collapse with almost immediate initiation of ensuing debris flows. Geomorphology 351, 106933. https://doi.org/10.1016/j.geomorph.2019.106933.
Weidick, A., 1987. Quaternary map of Greenland, sheet 1, Sydgrønland. 1:500,000. Geodætisk Institut, Danmark.
Weidick, A., Kelly, M., Bennike, O., 2004. Late Quaternary development of the southern sector of the Greenland Ice Sheet, with particular reference to the Qassimiut lobe. Boreas 33, 284–299. https://doi.org/10.1111/j.1502-3885.2004.tb01242.x.
Westoby, M.J., Brasington, J., Glasser, N.F., Hambrey, M.J., Reynolds, J.M., 2012. 'Structure-from-Motion' photogrammetry: a low-cost, effective tool for geoscience applications. Geomorphology 179, 300–314. https://doi.org/10.1016/j.geomorph.2012.08.021.
Winsor, K., Carlson, A.E., Caffee, M.W., Rood, D.H., 2015. Rapid last-deglacial thinning and retreat of the marine-terminating southwestern Greenland ice sheet. Earth Planet. Sci. Lett. 426, 1–12. https://doi.org/10.1016/j.epsl.2015.05.040.
Yoshida, H., Sugai, T., Ohmori, H., 2012. Size–distance relationships for hummocks on volcanic rockslide-debris avalanche deposits in Japan. Geomorphology 136, 76–87. https://doi.org/10.1016/j.geomorph.2011.04.044. Volcano Geomorphology: landforms, processes and hazards.
Young, N.E., Briner, J.P., Miller, G.H., Lesnek, A.J., Crump, S.E., Thomas, E.K., Pendleton, S.L., Cuzzone, J., Lamp, J., Zimmerman, S., Caffee, M., Schaefer, J.M., 2020. Deglaciation of the Greenland and Laurentide ice sheets interrupted by glacier advance during abrupt coolings. Quat. Sci. Rev. 229. https://doi.org/10.1016/j.quascirev.2019.106091.
Young, Nicolá.E., Schaefer, J.M., Briner, J.P., Goehring, B.M., 2013. A 10Be production-rate calibration for the Arctic. J. Quat. Sci. 28, 515–526. https://doi.org/10.1002/jqs.2642.